Rare Metal Materials and Engineering

Available online at **www.rmme.ac.cn**

Cite this article as: Rare Metal Materials and Engineering.

ARTICLE

DOI: 10.12442/j.issn.1002-185X.20240421.

Effect on microstructure and mechanical properties of new Nickel-based superalloys fabricated by selective laser melting at low energy density

He XU [1,2], Jingjing LIANG [1,2], Jinguo LI [1,2]

[1] School of Materials Science and Engineering, University of Science and Technology of China, Shenyang, 110016, China; [2] Shi-changxu Innovation Center for Advanced Materials, Institute of Metal Research, Chinese Academy of Sciences, Shenyang 110016, China

Abstract: In order to explore the effect of different energy densities on microstructure and mechanical properties of selective laser melting (SLM) formed ZGH401, ZGH401 was prepared under different laser power and scanning speeds by orthogonal test method by SLM. The microstructure of ZGH401 was analyzed by SEM, EBSD and EPMA. The results showed that the defects of the as-built ZGH401 were gradually reduced, and the relative density was gradually increased with the continuous increase of the energy density, and the final density can reach 99.6%. As the laser power increases, so did the hardness of ZGH401, and a quicker scanning speed reduced the remaining stress on the as-built ZGH401. In addition, better tensile properties at room temperature due to more grain boundaries parallel to the build direction than perpendicular direction. The precipitated phase was identified as carbides and Laves phases by its chemical composition, and the carbides at the molten pool boundaries were less than those in the melt pools.

Key words: Selective laser melting; Low energy density; ZGH401

Known as additive manufacturing (AM or 3D printing), this technique can create intricately shaped structures hard to or impossible to construct usual, marking it as a novel technical approach for producing superalloy components. While AM can overcome certain drawbacks of conventional methods, there remain fundamental issues to address prior to its mass application in industries. A significant concern is the residual stress and micro-cracks arising through heat during treatment. Several Ni-based superalloys are known to be prone to micro-cracking, barring their use in the production of aerospace parts[1, 2]. Selective laser melting is an additional manufacturing process that can produce samples quickly, cheaply and accurately with intricate geometric shapes. SLM is attracting increasing attention as an advanced biomedical device manufacturing method[3, 4].

Shahwaz M et al. provided a comprehensive overview of the effect of SLM on the organization evolution as well as properties of additively manufactured IN625 and IN718 alloys[5]. The main reason for the excellent properties of nickel-based high temperature alloys is due to the two reinforcing precipitation phases, γ′ (Ni_3Al) and γ″ (Ni_3Nb)[6-8]. At higher service temperatures, γ′ has a stronger thermal stability compared to the γ″ phase. The explanation given so far is that the effect of γ″ phase on the mechanical properties of alloys at high temperatures is superior to that of γ″ phase, possibly due to the transformation of γ" phase into δ phase at high temperatures, which reduces the mechanical properties of alloys[9-11]. Based on this, Al, Ti, Nb to promote the formation of strengthened phase, there are W, Mo can be solid solution strengthening of the matrix, rare earth elements to inhibit the γ′ phase coarsening, C, B can be added to increase the carbide at the grain boundaries, to prevent slippage, and to enhance the creep properties[12-14].

The layer-by-layer deposition, melting and solidification processes in the additive manufacturing process cause significant tissue evolution. Fish scale-like semicircular rings can be observed in different classes of additively fabricated nickel-based high temperature alloys[15-17]. These rings mainly in-

Received date:
Foundation item: 2021-JCJQ-JJ-0092
Corresponding author: Jinguo LI, Ph.D., Professor, Institute of Metal Research, Chinese Academy of Sciences, Shenyang 110016, P. R. China, Tel: 024-83978872, E-mail: jgli@imr.ac.cn
Jingjing LIANG, Ph.D., Professor, Institute of Metal Research, Chinese Academy of Sciences, Shenyang 110016, P. R. China, Tel: 024-23971787, E-mail: jjliang@imr.ac.cn

dicate the movement of the laser tip and subsequent formation of the melt pool. The opening spacing and layer thickness, as well as columnar versus equiaxed crystals can be seen in the molten pool morphology[18, 19]. The microstructure of a typical additively fabricated nickel-based high temperature alloy consists of a matrix, a reinforcing phase, MC-type carbides precipitated along grain boundaries, and a Laves phase consisting of Ti and Nb[20-22]. It is shown that the formation of the Laves phase is caused by the deviation of Nb. In order to obtain better properties and eliminate the residual thermal stresses during the additive manufacturing process, the microstructure of the alloy after the heat treatment of solution and annealing will have brittle needle-like δ-phase transformed by γ" at grain boundaries with Laves phase and $M_{23}C_6$ and M_6C decomposed by M carbides. The Laves phase is hard and brittle, and it is prone to cracking when stressed, whereas the δ-phase will reduce the γ-phase, and the Laves phase will decrease the δ-phase, which is composed of Ti and Nb. The δ phase will reduce the γ″ phase content, and the low-temperature organization uniformity and mechanical properties of the alloy can be improved by δ-phase solid solution treatment.

The ZGH401 is a high-performance nickel-based high-temperature alloy specially designed for additive manufacturing by the Institute of Metals, Chinese Academy of Sciences. Wu.B et al. had studied the preparation of ZGH401 made by laser metal deposition (LMD). The main components of the ZGH401 alloy are γ and γ' phases, as well as small amounts of Laves phase and MC carbides. The primary dendrite arm spacing (PDAS) for the deposited alloy measures approximately 15~50 μm, with an average γ' phase diameter ranging from 100~150 nm; in contrast, the as-cast alloy spans 300~500 μm and 200~350 nm. Reduced size of PDAS aids in the uniformity of alloys, prevents the creation of detrimental phases, significantly boosts the fortifying impact of alloy components, and betters their characteristics. In a broad processing range, the alloy that has been deposited remains intact without cracking. This alloy features a cellular dendrite that expands along the crystallographic direction [001], aligning with the direction of deposition. The elements Al, Cr, Co, and Nb, Ti shows a higher concentration in the dendrite core region and interdendritic region[23, 24].

However, although these studies have focused primarily on 3d printing of ZGH401. The current shortcomings are the lack of comprehensive in-depth systematic research on the organization and properties of the ZGH401 made by SLM. In order to enable the alloy to move from research and development to application and to provide support for the design of better alloys, this paper focuses on the study of the organization and morphology as well as the density, hardness, and residual stresses of the ZGH401prepared by SLM under low energy density.

1 Experiment

1.1 Powder properties

The chemical composition of ZGH401 is listed in Table 1. The powder was produced using vacuum-induced gas atomization at the Institute of Metal Research. ZGH401 powders consist of the following chemical compositions, measured in wt%: 20 wt% (Cr+Co), 9.2 wt% (Hf+Mo+Nb), 4.5 wt% (Al+Ti), 0.46 wt% (C+Si), bal. Ni.

Table 1 Element composition of alloys used in this study

Element	Al+Ti	Co+Cr	Hf+Mo+Nb	Si+C	Ni
Wt%	4.5	20	9.2	0.46	Bal.

The process of alloy powder preparation was as follows: according to the composition of Table 1, The alloy was melting ingot in a vacuum induction melting furnace to obtain the alloy bar, as material for the preparation of gas-atomize alloy powder, sieved out the powder with a particle size of 270-800 (diameter 18-53μm).

The ZGH401 powders are shown in Fig. 1. Most of the particles were spherical in shape, while only a few powders had satellite attachments. The average diameter of powders was 34.50 μm as shown in Fig. 1, In addition, D10=20.87μm, D50=35.79μm and D90=51.15μm. Inspect F50 scanning electron microscope (SEM) and Bettersize 2600 laser particle size distributor was used to assess the shape and size range of the powder.

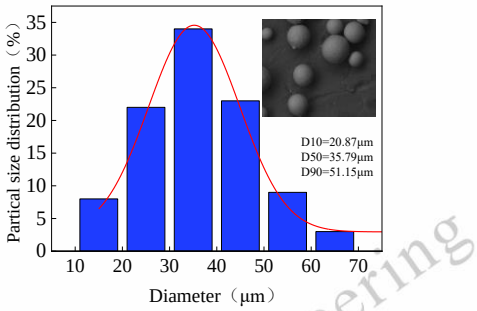

Fig. 1. SEM images of gas atomized ZGH401 powders and the diameter of powders

1.2 Sample preparation

Before proceeding with SLM, the ZGH401 powder underwent a 3-hour drying process at 200 °C. A Concept Laser M2 machine was utilized to conduct the SLM experiments. The SLM process took place under a highly pure Ar environment (with the oxygen content in the forming chamber below 0.1%), utilizing a 316L stainless steel plate as the base material for construction. Throughout the SLM procedure, the plate underwent preheating to 105 °C. The dimensions of the sample measured 15 × 15 × 20 mm^3, with its morphology depicted in Fig. 2 (a). In addition, in order to test the mechanical properties in different directions, two types of specimens were prepared as shown in Fig. 2(b) with dimensions of 20 × 20 × 55 mm^3. The parameters for the process were outlined below

listed in Table 2. The laser power (P) was 200, 220, 240, 260, 280, and 300 W. The thickness of the layer measured 50 μm, with a hatch spacing (h) of 120 μm. There was no angular rotation in the scanning approach between the neighboring layers (Fig. 2 (c)), and the speed of scanning was 750, 800, 850, 900, 950, and 1000 mm/s. From the above process parameters, energy densities in this SLM study can be calculated by Eq (1). The range of energy was between 33,33-66.67 J/mm^3.

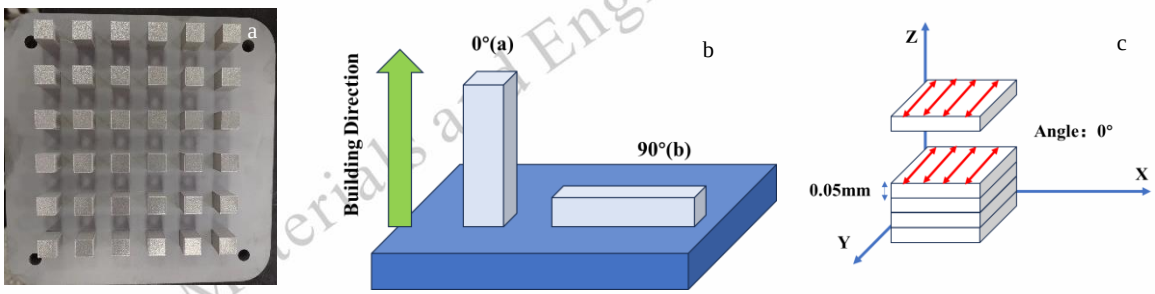

Fig. 2. (a) Smaller size samples and (b) two kinds of larger size samples in different orientations ;(c) scanning strategy

$$E=P/(v\cdot h\cdot d) \quad (1)$$

In Eq (1). E refers to the energy density (J/mm^3), P refers to the laser power (W), v refers to the scanning speed (mm/s), h refers to the hatch spacing (mm), and d refers to the layer thickness (mm).

Table 2 Process parameters used for the production of sample

P (W)	v (mm/s)	h (mm)	d (mm)	E (J/mm^3)
200-300	750-1000	0.12	0.05	33.33-66.67

After SLM, the specimen was cut from the substrate and the composition was analyzed using an X-ray fluorescence spectrometer and was found to be not too different from the initial powder composition.

1.3. Microstructure observation

The samples were produced in cubic forms measuring 15 mm× 15 mm× 20 mm. For cross-sectional analysis, the samples were sliced along the axis that aligns with the construction direction. Polishing of the sectioned area was achieved by #180, #240, #400, #800, #1000, and#2000 abrasive paper. The specimens were corroded using $CuCl_2$, HCl and C_2H_5OH. ZEISS Sigma-300 scanning electron microscopy (SEM) were used for observing the microstructure. Additional elemental analysis was performed by JXA-iHP20 Electron Probe Microanalysis (EPMA).

1.4. Properties measurement

The Vickers hardness measurement was tested at a load of 0.5 Kgf according to GB/T 4340.1-2009, under the condition of 23℃. The mean value was determined by assessing three specific points on the specimen's cross-sectional area. The specimens of 20mm×20 mm×55mm were cut from the substrate and processed into M6Φ3 specimens. The tensile tests were according to the plan B in GB/T 228.1-2021. Likewise, three sets of parallel specimens were tested. In addition, according to GB/T 31218-2014, the center point of the upper surface of the sample was tested by using KJS-3 (309001) residual stress tester.

2 Results and Discussion

2.1 Porosity

The energy density corresponding to each process was calculated by Equation 1, the samples were cut along the build direction, and the defects of the cross section were observed under OM as shown in Fig.3 The black dots in the figure represent the porosity, and the cross sections of 36 samples are arranged in order to obtain Fig.3 (a), which clearly reveals that the porosity of the samples increases as the scanning rate continues to increase, and the increase of the laser power causes the porosity to decrease, in other words, the energy density is the decisive factor affecting the porosity, and in this study, the higher the energy density, the smaller the porosity. This occurs because the laser's energy input remains minimal at low power levels, causing inadequate alignment between the melting and melting channels, and leading to partial melting of the alloy powder, causing issues like spherification and porosity. As the laser power intensifies, the powder within the melt pool completely dissolves, which makes the densities increase. When the scanning rate is too fast, resulting in an increase in the powder that is not fully melted, so that more pores are formed.

Analyzed by JMatPro software, the theoretical density of ZGH401 alloy is 8.24 g/cm^3. The density assessments were conducted in accordance with the renowned Archimedes' technique, ensuring a minimum of three repetitions per SLM sample. The result was shown in Fig. 3(b). It is clear that the difference in density is due to different porosities. Thus, to confirm the alignment between density measurements and the porosity of components made by SLM, using ImageJ software for image analysis, the precise space covered by internal porosities was determined in polished cross-sections of chosen samples, with the findings still presented in Fig. 3 (b). When the laser power is 200W and the scanning rate is 1000mm/s, the energy density of the alloy is only 33.33 J/mm^3 in Fig. 3

(c), the porosity reaches 5.8% and the density is only 7.91g/cm^3. And when the laser power is 300W and the scanning rate is 750mm/s, the energy density of the alloy is 66.66 J/mm^3 in Fig. 3(d). As the energy density increases from 33.33 J/mm^3 to 66.67 J/mm^3, the porosity decreases from more than 5% to less than 0.1%, and the density increases from 7.91 g/cm^3 to 8.21 g/cm^3, and we take the porosity of 0.1% as the cutoff point, which gives us an energy density of about 46 J/mm^3. If we want to obtain the alloy with qualified densities, we need to control the energy density above 46 J/mm^3 during the design process.

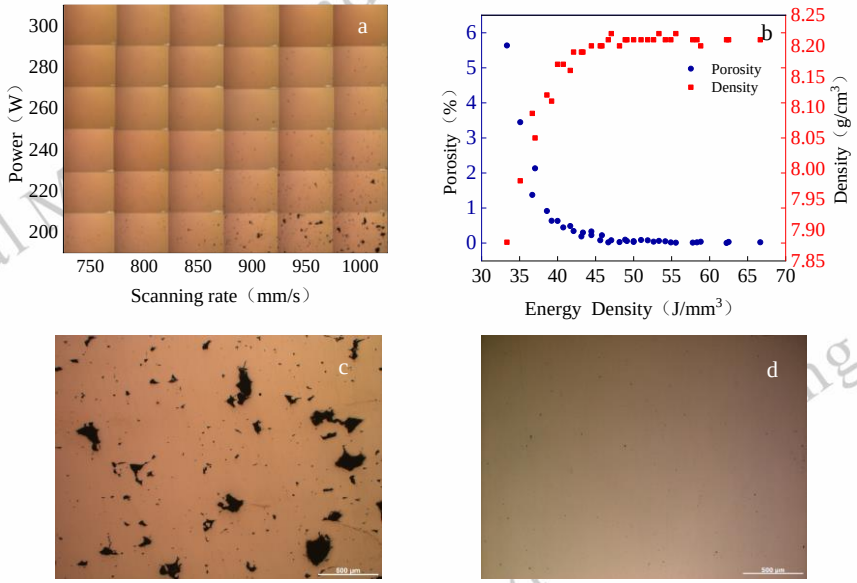

Fig. 3. (a) Morphology under different parameters; (c)200W, 1000mm/s; (d) 300W, 750mm/s;(b) Density and internal porosity of SLM samples

2.2. Hardness and residual stress

Fig. 4 shows the relationship between hardness with laser power and scanning rate during the optimization process of SLM ZGH401. It can be found that when the laser power is 300W and the scanning rate is from 800 to 1000mm/s, the hardness decreases from 362 to 349 HV. In the same pattern, the hardness decreases with increasing scanning rate when the laser power is 220 and 260W. Hardness increases with increasing laser power at a constant scanning rate.

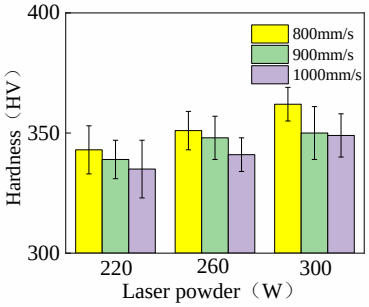

Fig. 4. Variation of hardness of ZGH401 with laser power and scanning rate

Hardness characterizes the ability of a material to resist local plastic deformation. When a large number of pores exist within an alloy, the pores collapse under external pressure and the alloy has a low hardness. As the bulk energy density increases, the number of pores decreases, and the hardness naturally increases.

Fig. 5 illustrates the outcomes of residual stress under varying energy density scenarios. Typically, the remaining stress attains 411.50MPa occasionally when laser power is minimal and scanning speed is maximal. At the peak of laser power and the lowest scanning speed, the mean residual stress reaches 359.50MPa.

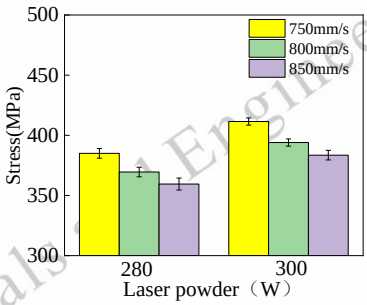

Fig. 5 Comparisons of residual stress in laser power with scanning rate

The duration of laser exposure to a particular region can lead to a rise in its temperature, ultimately influencing the rate at which the laser absorbs light. With the reduction in scanning velocity, there was a rise in the duration of laser exposure, consequently elevating both the temperature and the rate of

laser absorption. Consequently, there was a swift rise in thermal energy, hastening the thermal residual stress as the cooling process intensified. Scanning speed stands as the most variable parameter condition, and a reduction in this speed leads to heightened laser exposure and increased residual stress [25, 26].

2.3. Microstructure

The microstructures of SLM-formed specimens with different bulk energy densities are similar to those of the specimens with a bulk energy density of 66.67 J/mm3 for example. From Fig. 6 (a) can be seen: SLM formed ZGH401 alloy in the longitudinal cross-section of the fish scale morphology, these fish scales should be formed by the solidification of the molten pool, the same deposition layer scanning line between the lap is good, no porosity.

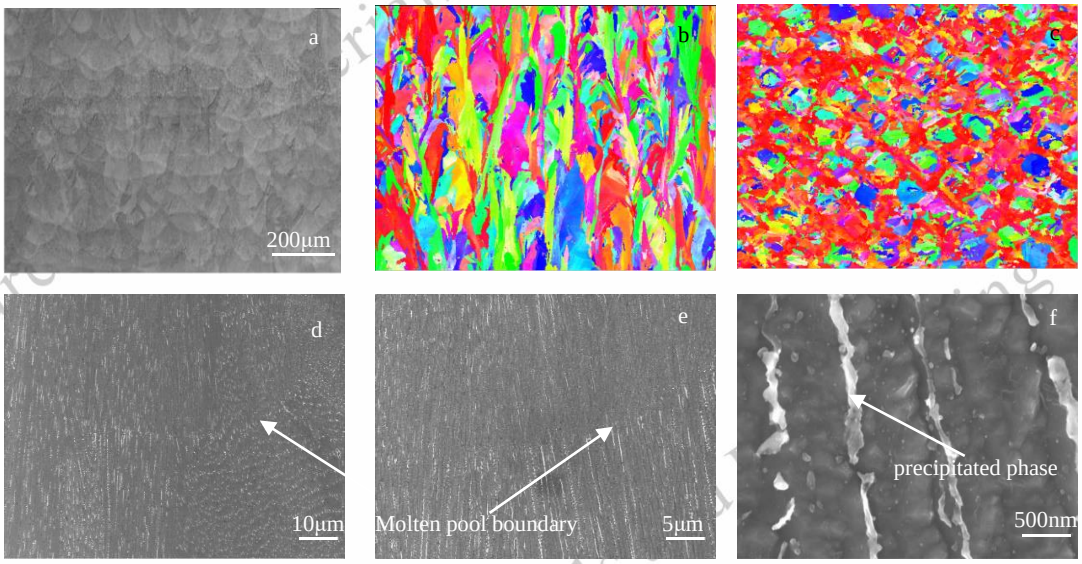

Fig. 6 (a);(b) Longitudinal section (perpendicular to the building direction) and (c) cross section by EBSD; (d), (e) and (f) Melt pool morphology by SEM

It can be seen from the comparison of Fig. 6 (b) and (c) that the columnar crystal of ZGH401 alloy grows along the crystallographic direction [001], aligning with the direction of deposition. During the production of ZGH401 samples with SLM, the energy input and cooling process result in the creation of columnar grains, accountable for the anisotropic mechanical characteristics of the samples as-build. Various process parameters together control the heat transfer process in additive manufacturing and influence the resulting anisotropic mechanical properties. Observing the intersecting semielliptical configuration of the molten pool was straightforward, with the melt pools' depths and widths recorded at 80 μm and 140 μm, in that order. It was observed that certain grains, measuring 30–80 μm in width, traverse several MPs in the constructed direction via epitaxial growth. An unbroken line measuring 0.1–0.2 μm in thickness, was positioned at the edges of the grains, which are expected to contain carbide precipitates. Comprising fine columnar and cellular sub grains, these sizable grains represent common solidification microstructures found in laser powder bed fusion-nickel-based superalloys. Spanning 0.5–1.5 μm in width and 6–16 μm in length, the columnar sub grain was lined with continuous thin layers or intermittent chains of particles. The majority of cellular sub-grains, averaging around 1.4 μm in size, were found near the boundaries of the molten pool, with a few carbide granules scattered along these cellular sub grain boundaries.

Table 3 Tensile strength at room temperature.

Samples	90°(MPa)	0°(MPa)	Gaps (MPa)
A	1150	1120	30
B	1146	1118	28
C	1148	1121	27
D	1159	1127	32
E	1138	1120	18
F	1136	1125	11
G	1157	1131	26
H	1160	1119	41
I	1139	1119	20
J	1143	1125	18

Fig. 7 shows the typical microstructures of the as-built ZGH401 sample along the build direction such as Hf; C; Si; Nb and Ti. Carbide precipitates. Elements that are heavily enriched are C and Nb. The rest of the elements (Hf; Si; and Ti) are only slightly enriched. We know that SLM-ed nickel-based superalloys consist of γ, γ' , carbides precipitated along grain boundaries, and a Laves phase consisting of Ti and Nb, and studies have shown that the formation of the Laves phase is

caused by the partial precipitation of Nb. From this, it can be hypothesized that this precipitated phase is composed of MC carbides that form sub grains together with grains in the construction direction, as well as Laves phase.

2.4. Mechanical properties

According to Fig. 2(b). The specimens of 20mm×20 mm×55mm were cut from the substrate and processed into M6Φ3 specimens. Two types of samples with different orientations were tested at the same time, which were 0° parallel to the direction of construction, and 90° perpendicular to the direction of construction. A total of 10 samples were tested and their tensile properties at room temperature are shown in Table 3. The maximum perpendicular to the direction of construction is 1160MPa. In addition to this, the performance of the two types of samples in different orientations under the same process was compared, resulting in a gap between the two orientations. The maximum and minimum gaps are 41MPa and 11MPa. The average is 25.10MPa.

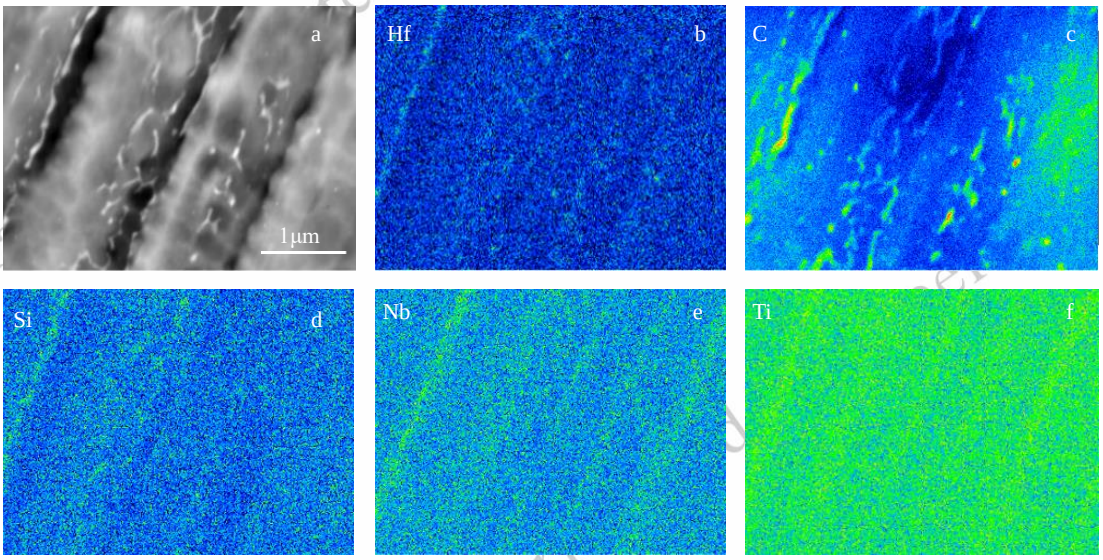

Fig. 7 Elemental distribution of ZGH401 as-built by EPMA
(a) Morphology; (b) Hf; (c) C; (d) Si; (e) Nb; (f) Ti

Samples parallel to the build direction are taller than those perpendicular to the build direction, requiring more layers and longer processing times, resulting in a higher probability of defect formation, which is thought to contribute to the poorer mechanical anisotropy and tensile properties of samples parallel to the build direction and a more important reason is that the grain boundaries parallel to the build direction are larger than those perpendicular to the build direction, which are thought to contribute to the poorer mechanical anisotropy and tensile properties of samples parallel to the build direction[27, 28]. Therefore, when using SLM to manufacture alloy parts, the build direction should be carefully considered in order to obtain excellent mechanical properties.

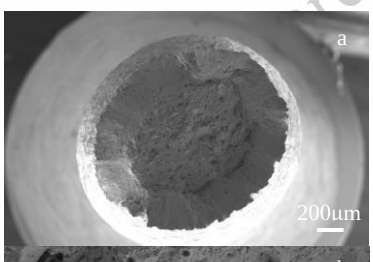

Fig. 8 Tension test results of ZGH401 as-built at 25℃

Fig. 8 shows the tension test results of ZGH401 as-built at 25℃. The fracture consists of a fiber zone and a shear lip zone, both of which are very distinct, both of which are ligamentous fossa fractures, and the depths of the ligamentous fossae are not very different.

3 Discussion

The SLM procedure involves a multifaceted process of

transferring heat. The intense energy emitted by the laser is conveyed to the powder layer, leading to the melting of the metal powder. During the additive manufacturing process, localized areas of the sample are rapidly warmed and cooled by hot endpoints, which tend to create temperature gradients, and the positional differences in this case lead to inconsistent expansion and contraction, which in turn generates large amounts of thermal stresses within the sample. Thermal stresses are an important source of residual stresses in the additive manufacturing process. During the heating phase, the thermal expansion of the newly deposited layer is limited by the previously solidified layer, resulting in compressive strains, and during the cooling phase, the contraction of the upper layer generates tensile residual stresses that can be balanced by compressive stresses in the surrounding region. Furthermore, as the metal sample is produced sequentially, the molten layers' solidification shrinkage overlays, creating tensile residual stresses on the uppermost layer's surface. When this phenomenon is applied across various layers, the residual stress on the surface of the specimen is usually tensile, which is also consistent with the results measured in this study. For alloys in the as deposited, either increasing the laser power or decreasing the scan rate will cause the temperature gradient to increase, resulting in residual stresses, so it can be argued that in determining one of these parameters, an increase in the energy density will indeed result in an increase in residual stresses.

In general, the main reasons for differences in specimen hardness should be analyzed in terms of cracks, holes, grains and the residual stress state of the alloy. The state of residual stress does affect the hardness, but for the specimen as-built, the grains under different energy densities will not change much, and the state of residual stress is also all tensile stress, only the value is different, in this case, the alloy contains some cracks and more micropores inside, and they have a greater effect on the hardness of the alloy, and the test will result in more deformations, and when the energy density is increased to a When the energy density in this study was increased to a certain degree, the cracks and some micropores were eliminated, and the internal tensile stress was in the opposite direction to the loading direction of the hardness tester, at this time, the greater the tensile stress, the greater the hardness performance, so in the alloy in the sedimentary state, it is not possible to satisfy both the reduced residual stress to increase the mechanical properties and the increase in the alloy hardness to enhance the resistance to deformation.

However, once the state of the residual stresses is changed, e.g., by subjecting the specimen to hot isostatic pressing, which causes the cracks to close all the way, the micropores to be reduced substantially, and the pressure applied to release most of the tensile stresses, more deformation will be resisted during testing. Can also change the grain state through heat treatment, play the role of grain boundary strengthening, while the grain has not grown and other phenomena, can also cause the hardness to improve. Therefore, ZGH401 alloy also has a high potential.

4 Outlook

Additively manufactured superalloys are at the forefront of materials research today. At present, there are a number of bottlenecks constraining the industrial application of additively manufactured superalloys, especially the crack sensitivity of superalloys. In response to these problems, the Institute of Metals, Chinese Academy of Sciences has developed a nickel-based superalloy ZGH401 specially designed for additive manufacturing, whose cracking can be effectively controlled. In the future, further research can be done on the organization and properties of ZGH401 after hot isostatic pressing, solid solution treatment and aging treatment, in order to obtain better microstructure and mechanical properties. At that time, ZGH401 may become an excellent nickel-based superalloy specialized in additive manufacturing, which in turn can provide theoretical and experimental support for the design and application of new additively manufactured superalloys.

5 Conclusions

In this paper, ZGH401 alloy was prepared by SLM at different energy density (33.3~66.6 J/mm^3). The influence of laser power and scanning speed on the densification behavior, microstructure, Vickers hardness, and tensile properties was studied systematically, and the following conclusions were obtained.

1) With the increase of laser power, the powder in the melt pool is fully melted, which makes the densities increase. When the scanning rate is too fast, resulting in an increase in the powder that is not fully melted, so that more pores are formed. As the energy density increases from 33.33 J/mm^3 to 66.67 J/mm^3, the porosity decreases from more than 5% to less than 0.1%, and the density increases from 7.91 g/cm^3 to 8.21 g/cm^3.

2) It can be found that hardness increases with increasing laser power at a constant scanning rate. On average, the residual stress reaches 411.50MPa at times when laser power is minimal and scanning speed is maximal. At the peak of laser power and the lowest scanning speed, the mean residual stress reaches 359.50MPa.

3) SLM formed ZGH401 alloy in the longitudinal cross-section of the fish scale morphology, these fish scales should be formed by the solidification of the molten pool, the same deposition layer scanning line between the lap is good, no porosity.

4) The chemical composition of the precipitates is determined to be carbides that form sub grains together with grains in the construction direction and Laves phases, and the precipitates at the boundary of the molten pool are less than those in the molten pool.

5) Mainly due to the number of grain boundaries, the tensile

properties parallel to the build direction are poorer than those in the perpendicular direction. The average of them are 1146.5MPa，1122.5 MPa, respectively. The maximum and minimum gaps are 41MPa and 11MPa. The average of the gaps is 25.10MPa.

6 Acknowledgements

This study was supported by the National Defense Science and Technology Project Management Center for the financial support grant no. 2021-JCJQ-JJ-0092.

References

1. Bang G B , Park J H , Kim W R ,et al.Study on the effect of preheating temperature of SLM process on characteristics of CoCrMo alloy[J]. *Materials Science and Engineering: A*,. Structural Materials: Properties, Misrostructure and Processing, 2022:841.
2. Zhang Min, Ma Chuanchuan, Xue Chun, et al. Effect of Precipitate Phases and Grain Size on Mechanical Properties of Inconel 718 Superalloy After Various Heat Treatments[J]. Rare Metal Materials and Engineering, 2024, 53(08): 2131-2136.
3. Chen Shuang, Yang Yanhong, Guo Zhiqiang, et al. Influence of Post-Treatment Process on Microstructure and Properties of Laser Additively Manufactured Nickel-Based Superalloy[J]. Rare Metal Materials and Engineering, 2024, 53(09): 2478-2484.
4. Wang C, Hu Y, Zhong C, et al. Microstructural evolution and mechanical properties of pure Zn fabricated by selective laser melting[J]. *Materials Science and Engineering: A*, 2022, 846: 143276.
5. Shahwaz M, Nath P, Sen I. A critical review on the microstructure and mechanical properties correlation of additively manufactured nickel-based superalloys[J]. *Journal of Alloys and Compounds*, 2022, 907: 164530.
6. Macoretta G, Monelli B D. SLM process parameters effects on the fatigue strength of AMed Inconel 718[J]. *Procedia Structural Integrity*, 2022, 37: 632-643.
7. Periane S, Duchosal A, Vaudreuil S, et al. Influence of heat treatment on the fatigue resistance of Inconel 718 fabricated by selective laser melting (SLM)[J]. *Materials Today: Proceedings*, 2021, 46: 7860-7865.
8. Li M, Wang L, Yang H, et al. Microstructure and mechanical properties of Y2O3 strengthened Inconel 625 alloy fabricated by selective laser melting[J]. *Materials Science and Engineering: A*, 2022, 854: 143813.
9. Ren D, Xue Z, Jiang Y, et al. Influence of single tensile overload on fatigue crack propagation behavior of the selective laser melting inconel 625 superalloy[J]. *Engineering Fracture Mechanics*, 2020, 239: 107305.
10. Chen L, Gu P, Ge T, et al. Effect of laser shock peening on microstructure and mechanical properties of TiC strengthened inconel 625 alloy processed by selective laser melting[J]. *Materials Science and Engineering: A*, 2022, 835: 142610.
11. Chen F, Wang Q, Zhang C, et al. Microstructures and mechanical behaviors of additive manufactured Inconel 625 alloys via selective laser melting and laser engineered net shaping [J]. *Journal of Alloys and Compounds*, 2022, 917: 165572.
12. Huang W, Li Y, Yanjie R E N, et al. Effect of scanning speed on the high-temperature oxidation resistance and mechanical properties of Inconel 625 alloys fabricated by selective laser melting[J]. *Vacuum*, 2022, 206: 111447.
13. Karabulut Y, Tascioglu E, Kaynak Y. Heat treatment temperature-induced microstructure, microhardness and wear resistance of Inconel 718 produced by selective laser melting additive manufacturing[J]. *Optik*, 2021, 227: 163907.
14. Pu Yunna, Zhao Dewei, Liu Binbin, et al. Microstructure Evolution and Mechanical Properties of Ti-25Ta Alloy Fabricated by Selective Laser Melting and Hot Isostatic Pressing[J]. Rare Metal Materials and Engineering, 2024, 53(08): 2123-2130.
15. Dong X, Zhou Y, Qu Y, et al. Recrystallization behavior and grain boundary character evolution in Co-Cr alloy from selective laser melting to heat treatment[J]. *Materials Characterization*, 2022, 185: 111716.
16. Hu T, Li W, Yuan S, et al. Multiscale analysis of interior cracking behavior of Ni-based superalloy fabricated by selective laser melting under very-high-cycle-fatigue at high-temperature[J]. *Materials Today Communications*, 2022, 33: 104356.
17. Hu Y, Dong C, Kong D, et al. Effects of post-production heat treatment on the mechanical and corrosion behaviour of CoCrMoW alloy manufactured through selective laser melting[J]. *Materials Today Communications*, 2021, 29: 102994.
18. Karimi J, Kollo L, Rahmani R, et al. Selective laser melting of in-situ CoCrFeMnNi high entropy alloy: Effect of remelting[J]. *Journal of Manufacturing Processes*, 2022, 84: 55-63.
19. Park J M, Kim E S, Kwon H, et al. Effect of heat treatment on microstructural heterogeneity and mechanical properties of 1% C-CoCrFeMnNi alloy fabricated by selective laser melting[J]. *Additive Manufacturing*, 2021, 47: 102283.
20. Tan Q, Zhu G, Zhou W, et al. Precipitation, transformation, and coarsening of carbides in a high-carbon Ni-based superalloy during selective laser melting and hot isostatic pressing processes[J]. *Journal of Alloys and Compounds*, 2022, 913: 165196.
21. Lee J U, Kim Y K, Seo S M, et al. Effects of hot isostatic pressing treatment on the microstructure and tensile properties of Ni-based superalloy CM247LC manufactured by selective laser melting[J]. *Materials Science and Engineering: A*, 2022, 841: 143083.
22. Li B, Du J, Sun Y, et al. On the importance of heat source model determination for numerical modeling of selective laser melting of IN625[J]. *Optics & Laser Technology*, 2023, 158: 108806.
23. Wu B, Liang J, Yang Y, et al. Phase constitution, microstructure and mechanical properties of a Ni-based superalloy specially designed for additive manufacturing[J]. *China Foundry*,, 2021, 18: 397-408.

24. Bin W U, LIANG J, ZHOU Y, et al. Influence of laser power on microstructure and tensile property of a new nickel-based superalloy designed for additive manufacturing[J]. *Transactions of Nonferrous Metals Society of China*, 2023, 33(4): 1124-1143.
25. Ko K H, Kang H G, Huh Y H, et al. Effects of heat treatment on the microstructure, residual stress, and mechanical properties of Co–Cr alloy fabricated by selective laser melting[J]. *Journal of the Mechanical Behavior of Biomedical Materials*, 2022, 126: 105051.
26. Lan L, Wang W, Cui Z, et al. Effect of scanning speed on microstructure and mechanical properties of selective laser melting AlCoCrFeNi2. 1 eutectic high-entropy alloy[J]. *Materials Letters*, 2023, 330: 133321.
27. Ding R G, Zheng J P, Zhang Y Z, et al. Microstructure and mechanical properties of direct laser deposited DD98 superalloy[J]. *Materials Science and Engineering: A*, 2022, 848: 143427.
28. Huang Y, Xie Z, Li W, et al. Dynamic mechanical properties of the selective laser melting NiCrFeCoMo0. 2 high entropy alloy and the microstructure of molten pool[J]. *Journal of Alloys and Compounds*, 2022, 927: 167011.

低能量密度对选区激光熔化制备新型镍基高温合金的组织和性能的影响研究

徐鹤[1,2]，梁静静[1,2]，李金国[1,2]

(1. 中国科学技术大学材料科学与工程学院，辽宁 沈阳 110016)

(2. 中国科学院金属研究所师昌绪先进材料创新中心，辽宁 沈阳 110016)

摘　要：为了探讨不同能量密度对选区激光熔化 ZGH401 合金的显微组织和力学性能的影响，采用 SLM 正交试验方法，在不同激光功率和扫描速度下制备了 ZGH401。采用 SEM、EBSD 和 EPMA 对 ZGH401 的微观结构进行了分析。结果表明:随着能量密度的不断增大，沉积态 ZGH401 的缺陷逐渐减少，相对密度逐渐增大，最终密度可达 99.6%，随着激光功率的增加，ZGH401 的硬度也随之增加，同时更快的扫描速度也降低了 ZGH401 合金的残余应力。此外，由于垂直沉积方向的晶界相比平行沉积方向的更多，因此室温拉伸性能也更优异。析出相主要为碳化物和 Laves 相，熔池边界处的碳化物少于熔池内的碳化物。

关键词：选区激光熔化; ZGH401; 低能量密度

作者简介：徐鹤，男，1997 年生，博士，中国科学院金属研究所师昌绪先进材料创新中心，辽宁 沈阳 110016，电话：18811512707，E-mail: xuhe1997@126.com